Buckling-induced encapsulation of structured elastic shells under pressure

Jongmin Shim[a,1], Claude Perdigou[b], Elizabeth R. Chen[c], Katia Bertoldi[a,1,2], and Pedro M. Reis[b,1,2]

[a]School of Engineering and Applied Sciences, Harvard University, Cambridge, MA 021383; [b]Departments of Mechanical Engineering and Civil and Environmental Engineering, Massachusetts Institute of Technology, Cambridge, MA 02139; and [c]Department of Mathematics, University of Michigan, Ann Arbor, MI 48109

Edited by* John W. Hutchinson, Harvard University, Cambridge, MA, and approved January 9, 2012 (received for review September 22, 2011)

We introduce a class of continuum shell structures, the Buckliball, which undergoes a structural transformation induced by buckling under pressure loading. The geometry of the Buckliball comprises a spherical shell patterned with a regular array of circular voids. In order for the pattern transformation to be induced by buckling, the possible number and arrangement of these voids are found to be restricted to five specific configurations. Below a critical internal pressure, the narrow ligaments between the voids buckle, leading to a cooperative buckling cascade of the skeleton of the ball. This ligament buckling leads to closure of the voids and a reduction of the total volume of the shell by up to 54%, while remaining spherical, thereby opening the possibility of encapsulation. We use a combination of precision desktop-scale experiments, finite element simulations, and scaling analyses to explore the underlying mechanics of these foldable structures, finding excellent qualitative and quantitative agreement. Given that this folding mechanism is induced by a mechanical instability, our Buckliball opens the possibility for reversible encapsulation, over a wide range of length scales.

Jitterbug | deployable structure

Advances in fabrication technology are enabling functional origami-like structures at the nano- and microscales (1–3), including encapsulation using hollow shell structures (4–7). In engineering, these structures are receiving increasing attention for their promising role as vehicles for drug delivery (8), material synthesis agents (9), optical devices (10), and sensors (11). An interesting avenue is the introduction of gating (also known as actuation) mechanisms into such capsules by incorporating functional elements into their structural layout toward tunable encapsulation. Coupling conventional actuation mechanisms at the microscale (including electromagnetic, piezoelectric, thermal, electrochemical, rheological) with buckling may lead to unique or more efficient functional modes of deformation (12, 13). As an example, the Venus flytrap combines a swelling mechanism with buckling behavior to increase the speed of leaf motility (14, 15). Also, an active microhydrogel device was recently designed for dynamic actuation using a swelling-induced elastic instability (16).

There are a few existing hollow shell structures which have gating mechanisms, albeit not driven by buckling. Viruses are an ubiquitous class of such examples in nature. Their capsids possess a spherical shell structure that encloses and transports viral nucleic acids (17, 18) and can undergo reversible structural transformations by which gated holes can open or close under pH changes (18). This transformation occurs due to the expansion of the vertices of the truncated icosahedral structure of the virus, resulting in 60 hole openings. Using this deployable capability, viruses have been used as protein cages for encapsulation (19). In order to describe the virus swelling/shrinking behavior, Kovács et al. investigated the possible geometric compatibility with polyhedral models (20, 21).

The Jitterbug, introduced by R. Buckminster Fuller in the 1960s, is another example of a hollow shell structure satisfying geometric compatibility for gating holes. It enables the morphing between an octahedron and a cuboctahedron (22), thereby imparting flexibility to otherwise rigid grid structures. Since then, a number of studies have generalized the understanding of Jitterbug-like motion (face rotations at the vertices) through polyhedral transformations (23–25). These provide a robust set of rules for the design of spherical deployable structures that can fully close into their collapsed state. A popular commercial toy, Hoberman's Twist-o (Hoberman Associates) (26) which comprises a rigid network of struts connected by rotating hinges (Fig. 1*A*), also morphs from an open grid shell into a collapsed configuration. One drawback of these configurations toward practical applications is that the deformation is localized at the vertices of the polyhedra and a large number of hinges and rotating elements is required to achieve the intended motion.

Here, motivated by these opportunities for augmented motion and deformation of structures, we explore buckling as a possible gating mechanism for structured spherical shells. Our shells are patterned with a regular array of circular voids and loaded by reducing the internal pressure. Below a critical pressure, the narrow ligaments between the voids buckle, leading to a cooperative buckling cascade of the skeleton of the ball. We exploit this pattern transformation that leads to closure of all the holes, which is analogous to a structural negative Poisson's ratio effect previously studied in two dimensions (27), but now on a three-dimensional structure. Because our patterned shell has a geometry reminiscent of a buckyball (28) and, moreover, it can be activated by buckling, we name it the Buckliball. We first show the results of a combination of desktop-scaled experiments (Fig. 1*B*) and finite element (FE) simulations (Fig. 1*C*) on encapsulation through pressure-induced buckling of spherical shells. For the sake of experimental convenience and accurate control, we choose pressure as the actuation mechanism for the Buckliball. Consequently, thin membranes covering the holes are introduced in our samples to enable us to readily load the structure. Because the numerical results reveal that the characteristic deformation modes are only marginally affected by the presence of the membranes, for the sake of generality we then focus on the skeleton of the Buckliball without membranes over the voids and identify the underlying mechanical ingredients. Finally, through a scaling analysis, we provide a master curve for design guidelines of this class of structures.

Experimental Results

Inspired by the construction and motion of the rigid toy in Fig. 1*A*, we have made use of rapid prototyping techniques to fabricate a continuum version of the spherical grid shell made of a soft

Author contributions: J.S., K.B., and P.M.R. designed research; J.S., C.P., E.R.C., K.B., and P.M.R. performed research; J.S. analyzed data; and J.S., K.B., and P.M.R. wrote the paper.

The authors declare no conflict of interest.

*This Direct Submission article had a prearranged editor.

[1]J.S., K.B., and P.M.R contributed equally to this work.

[2]To whom correspondence may be addressed. E-mail: bertoldi@seas.harvard.edu and preis@mit.edu.

This article contains supporting information online at www.pnas.org/lookup/suppl/doi:10.1073/pnas.1115674109/-/DCSupplemental.

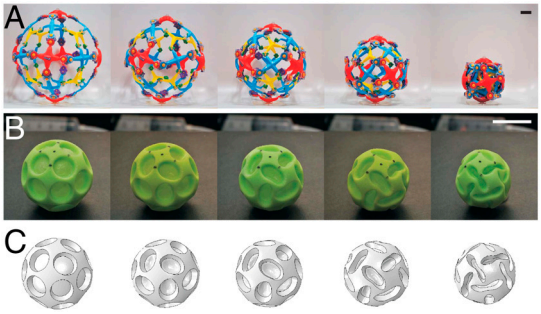

Fig. 1. Sequence of progressively deformed shapes. (*A*) Hoberman's Twist-o, a commercial toy, compressed by hand. (*B*) Buckliball, made of silicone-based rubber, pressurized by a motorized syringe pump. (*C*) Finite element simulations for the Buckliball. (Scale bars: 3 cm.)

silicone-based rubber (Vinylpolysiloxane with Young's modulus, $E = 784$ kPa). The geometry of the spherical elastomeric structure (inner radius $R_i = 22.5$ mm) comprises a shell (wall thickness $t = 5$ mm) that is patterned with a regular array of 24 circular voids that are slightly tapered (17 and 14 mm maximum and minimum diameter, respectively). The voids are distributed in groups of three on each one-eighth of the sphere. A thin membrane (thickness $h = 0.4 \pm 0.1$ mm) covering all the holes is introduced, to make the structure airtight, which provides the continuum shell with a means of pressure-induced actuation. This thin membrane allows for an isotropic loading through a distributed pressure difference between the inside and outside of the structure. More details of the manufacturing and experimental procedures are given in *Materials and Methods*.

The experiments are performed under conditions of imposed volume using a motorized syringe pump (see *Materials and Methods*). When the internal pressure is larger than the external pressure, the structure inflates like a balloon. Conversely, upon reduction of the internal pressure (see *Materials and Methods*), the behavior is qualitatively different. First, the thin membranes snap-buckle and invert their curvature inward. Subsequently, beyond a critical pressure, the narrow ligaments between the holes buckle on the spherical surface, leading to a cooperative buckling cascade of the skeleton of the ball. During this process, the initially circular holes evolve into an elliptical shape and eventually become fully closed. The sequence of progressive deformed shapes is shown in Fig. 1*B*. It is interesting to note that this final pattern closely resembles the recent work of Li et al. (29) reporting a surface wrinkling pattern of a core-shell soft sphere by volumetric shrinkage, although the structural details of the two systems are fundamentally different.

In order to monitor the rotation of the narrow ligaments, four black dots are marked at the center of each strut (on the top of the shell's surface) and then tracked with digital imaging. In Fig. 2*A*, we plot the averaged trajectory of these four dots (solid black line) which show that each ligament rotates clockwise by approximately 75° until the holes are nearly closed. In addition, we image the shell's projection from above, as its internal pressure is reduced, and monitor its outer radius. Fig. 2*B* (solid black line) presents the dependence of the measured pressure p and the nominal outer radial strain u/R_o, where R_o is the initial outer radius and u is the outer radial displacement. Two distinct regimes are identified: (*i*) a linear regime with positive structural stiffness for small deformations and (*ii*) a postbuckling regime with negative structural stiffness.

Because the structure is made of an elastomeric material, the process is fully reversible/repeatable, and upon a decrease in pressure difference, the structure recovers to its original configuration, albeit with hysteresis. Note that all the deformation occurs on a spherical surface with progressively decreasing dimensions, thereby preserving the original spherical geometry.

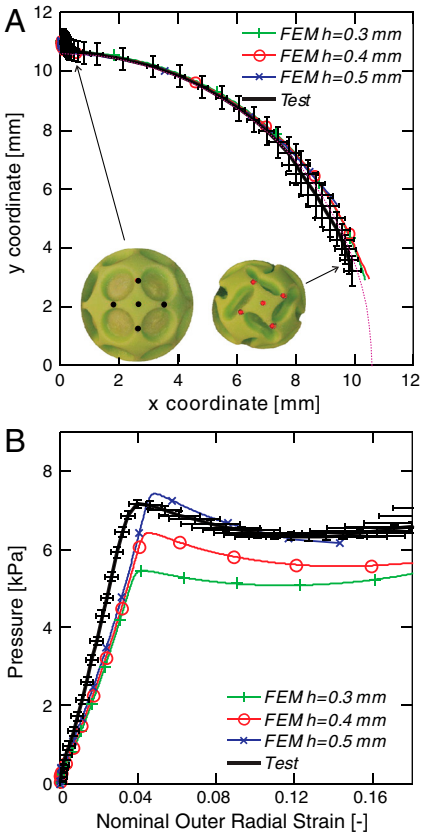

Fig. 2. Experimental and numerical results for the Buckliball. Note that each set of data reported in the figure is obtained from a single test, and all the numerical results are obtained using finite element modeling (FEM). (*A*) Average rotation of the ligament traced by four black dots which are marked on the top of the shell's surface (*Inset*). The error bars represent the standard deviation for these four ligaments rotations. (*B*) Relation between the differential pressure of the ball and the nominal outer radial strain (defined by the measured outer radial displacement divided by the initial outer radius). The horizontal error bar for the radial strain is obtained from image processing analysis, and the vertical error bar for the pressure is obtained from pressure measurement reading during multistep volume control.

An abrupt out-of-sphere buckling (snap buckling), which is highly sensitive to imperfections (30, 31), can occur instead of our intended on-sphere buckling, if the geometry and dimension of the spherical shells are not accurately designed.

Finite Element Analysis

We proceed by performing FE simulations to explore the encapsulation behavior of the proposed shell structure. Because the experiments are performed at imposed volume, volume-controlled conditions are used in the simulations. More details of the FE simulations are given in *Materials and Methods* and the *SI Text*. We present a sequence of the progressive collapse of a Buckliball obtained using FE simulations (Fig. 1*C*), which is in remarkable qualitative agreement with experiments (Fig. 1*B*) for the same geometric and material parameters. Moreover, there is excellent quantitative agreement between experiments and simulations, on the rotation of the shell ligaments (Fig. 2*A*).

In order to consider the variation of the measured membrane thickness of the experimental specimen (set by the resolution of the manufacturing process), simulations were performed with three different membrane thicknesses (i.e., $h = 0.3, 0.4, 0.5$ mm). Simulations for these three values of the membrane thickness do not show a pronounced difference on the deformed shapes, but they do, however, slightly affect the critical buckling pressure due to the additional structural stiffness associated with thicker

ENGINEERING

membranes. Still, for the dependence of the applied pressure on the outer radial strain presented in Fig. 2*B*, all three sets of simulation results are in good agreement with the experimental results in the linear regime. Excellent agreement between experiments and simulation is found for $h = 0.5$ mm, even though the effect of the membrane thickness becomes more pronounced at the onset of buckling. Note that this small discrepancy is attributed to limitations in the accuracy of the membrane thickness due to the fabrication process (see *Materials and Methods*).

Given the excellent qualitative and quantitative agreement found between experiments and simulations, we now proceed by focusing primarily on the FE simulation results to further explore the parameter space of the system and probe the underlying mechanical ingredients of this buckling-induced pattern transformation.

Mechanical Ingredients

Thus far, we have demonstrated proof-of-concept of the Buckliball through a combination of experiments and FE simulations, for the on-sphere buckling induced by pressure. Moreover, the above numerical results suggest that the characteristic deformation modes are only marginally affected by the presence of the membrane, given that the membrane thickness is considerably smaller than any other length scale in the system.

Therefore, for the sake of generality and to seek understanding of the essential features of the proposed encapsulation mechanism, we proceed by focusing on the Buckliball without membranes covering the holes. The original total force previously acting on the Buckliball with membranes covering the holes is now redistributed on the inner surface of the skeleton alone (i.e., Buckliball without membranes covering the holes).

We now investigate the two principal mechanical ingredients: geometric compatibility and gating mechanism. In particular, we first concentrate on the arrangement of holes to uncover other possible configurations that also lead to the desired encapsulation behavior, in addition to the one mentioned above (Fig. 1), and then focus on predicting the buckling loads and modes. To help us refer to the specific deformation modes of the spherical shells, we use the terms "expanded" and "folded status" to describe the configurations of the ball with open (undeformed) and closed holes (past the instability), respectively.

Arrangement of the Holes. The set of rules for geometric compatibility of Jitterbug-like polyhedra has been investigated previously (23, 24), and Verheyen has reported the complete list of Jitterbug-like transformations (25). In light of these studies, we also explore the hole arrangement on our spherical shells through polyhedra. Here, we consider continuum spherical shells where all the center-to-center distance of adjacent holes are identical so that all ligaments undergo the first buckling mode in an approximately uniform manner, restricting the number of the possible candidates from the complete list of Verheyen.

In order for all the ligaments between neighboring circular holes to undergo a uniform first buckling mode, the folded status should meet the following requirements: (*a*) The same shaped holes should be equally distributed on the spherical shells, and (*b*) all the circular holes should close uniformly and completely. Mathematically, these mechanical constraints can be rephrased as follows: The skeleton of the Buckliball should (*a′*) be a convex uniform polyhedra, excluding the dihedral symmetry group (i.e., Platonic/Archimedean solids, ref. 32), which are vertex transitive and have regular faces, and (*b′*) have a quadrilateral vertex figure. There are only five polyhedra which meet the above requirements: octahedron, cuboctahedron, rhombicuboctahedron, icosidodecahedron, and rhombicosidodecahedron, which can produce (upon face rotations at the vertices) the square-type holes of 6, 12, 24, 30, and 60, respectively. These, and only these, ensure that all the ligaments in the expanded status undergo the first buckling mode uniformly.

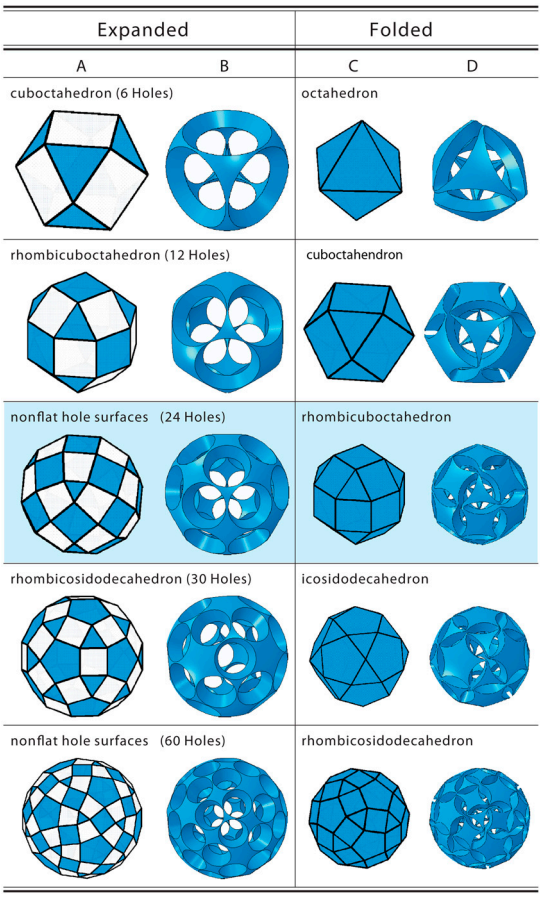

Fig. 3. Geometric compatibility for the arrangement of circular holes on the Buckliballs, restricted to five specific configurations (shown in each row). (*A*) Expanded Buckliball-related polyhedra: The blue-shaded area corresponds to solid regions and the white area corresponds to holes. (*B*) Expanded undeformed Buckliballs. (*C*) Folded Buckliball-related polyhedra. (*D*) Folded Buckliballs, which are buckled under inward pressure. Two of the solids in *A* (i.e., expanded status of the folded rhombicuboctahedron and rhombicosidodecahedron) have nonflat faces for the holes. Those two structures are transformed into polyhedra in their folded status by closing the nonflat holes.

In Fig. 3, we present schematic diagrams of the five possible polyhedra on the expanded (Fig. 3*A*) and folded (Fig. 3*C*) status. In the figure, the blue-shaded faces of the polyhedra represent the solid parts of the corresponding physical structure and the white faces of the expanded status represent the holes that undergo the transformation. As an example, an octahedron in the folded status can be expanded into a cuboctahedron through face rotations at the vertices, thereby producing six holes, which corresponds to the number of vertices of the octahedron. Note that the cuboctahedron in the expanded status is the famous Jitterbug introduced by Fuller (22) mentioned above.

In connection with the polyhedra models of expanded status, three-dimensional representations of the initially expanded spherical shells (Fig. 3*B*) can be obtained by introducing circular voids such that two neighboring holes create a narrow ligament at the vertex location of the corresponding polyhedron. Fig. 3*D* also shows the on-sphere buckled shapes for all five possible arrangements of the folded status of spherical shells, which are obtained through buckling analysis using FE simulations.

Buckling of the Ligaments. Having identified the geometrical constraints of the Buckliball configurations, we now explore the design parameters that lead to the desired gating mechanism for activation under pressure, through simultaneous buckling of all ligaments on a spherical surface. For a given hole configuration,

the proposed spherical shells have two dimensionless design parameters: the ratio of the shell thickness to the inner radius,

$$\tau = \frac{t}{R_i}, \qquad [1]$$

and the ratio of the void volume to the intact shell volume,

$$\psi = \frac{N}{2}\left[1 - \cos\left(\frac{\phi - \alpha}{2}\right)\right], \qquad [2]$$

where N is the number of holes for the corresponding polyhedron, α is the angle which defines the narrowest width of the ligament, and ϕ is the angle between two vectors that originate at the shell center and terminate at two neighboring vertices of a folded polyhedron (see Fig. 4 *A* and *B*). Because the void's center in the expanded polyhedron is placed at the vertex locations of the folded polyhedron, ϕ also represents the angle relating the center-to-center distance between two adjacent circular voids in the expanded polyhedron (see *SI Text* for details). Note that both N and ϕ are fixed for a particular hole configuration and the possible pairs for the five configurations mentioned above are $\langle N, \phi\rangle = \langle 6, \frac{\pi}{2}\rangle$, $\langle 12, \frac{\pi}{3}\rangle$, $\left\langle 24, \cos^{-1}\left(\frac{3+2\sqrt{2}}{5+2\sqrt{2}}\right)\right\rangle$, $\langle 30, \frac{\pi}{5}\rangle$, and $\left\langle 60, \cos^{-1}\left(\frac{9+4\sqrt{5}}{11+4\sqrt{5}}\right)\right\rangle$. The two additional design parameters $\langle \tau, \psi\rangle$ prescribe the dimensions of the narrow ligaments which undergo buckling, thereby setting the threshold of the activation.

As observed in the experiments, the narrowest cross-section of ligament in the expanded status of the spherical shells governs the behavior of the on-sphere buckling of the ball. For this on-sphere buckling to happen, the second moment of area along the radial axis should be smaller than that along the perpendicular axis—i.e., $I_{rr} \le I_{\theta\theta}$ (see Fig. 4*B*). The dimension of the narrowest cross-section of ligament is determined by τ and α, so that the restricting condition on the second moment of area reads

$$\frac{(\tau^2 + 3\tau + 3)^2}{(\tau + 2)^2(\tau^2 + 2\tau + 2)} = \frac{9\alpha \sin\alpha}{16(1 - \cos\alpha)}, \qquad [3]$$

where α is given by Eq. **2**. Together, Eqs. **2** and **3** provide a relation between the two design parameters $\langle \tau, \psi\rangle$, which is set by the particular hole arrangement alone—i.e., $\langle N, \phi\rangle$. As examples, in Fig. 4 *C* and *D*, we plot (dotted marked line) the design boundary set by Eqs. **2** and **3** for the spherical shells with 12 and 24 holes, respectively. Above this line, the Buckliballs are activated through the intended on-sphere buckling mode, whereas below it, other out-of-sphere (snap) buckling modes occur.

Comparison with FE Simulations. To assess our predictions on the effect of the hole arrangement and design parameters on ligament buckling, we perform a parametric study using FE simulations for the buckling analysis. FE models of the initially expanded spherical shells, for the five possible hole arrangements, are presented in Fig. 3*B*, to which an inward pressure is applied. For all five configurations, we perform a series of FE simulations on the design parameters $\langle \tau, \psi\rangle$. Representative results for shells with 12 and 24 holes are presented in Fig. 4 *C* and *D* as contour maps. In these phase diagrams, regions where out-of-sphere (snap) buckling occurs are represented in white. In the shaded regions where encapsulation (i.e., on-sphere buckling) occurs, the color in the contour plots represents the associated critical buckling pressure for onset of on-sphere buckling (normalized by the Young's modulus E), given by the adjacent color bar. Representative examples of the calculated final on-sphere buckled shapes for all five possible arrangements on the folded status are also presented in Fig. 3*D*.

For a given hole configuration, this parametric study reveals that thicker shells and higher void volume fraction are preferable to make the Buckliball buckle on sphere. We highlight that the contour map boundary between the regions of on-sphere and out-of-sphere buckling is in good agreement with our criterion of design parameters (dashed marked line) based on the second

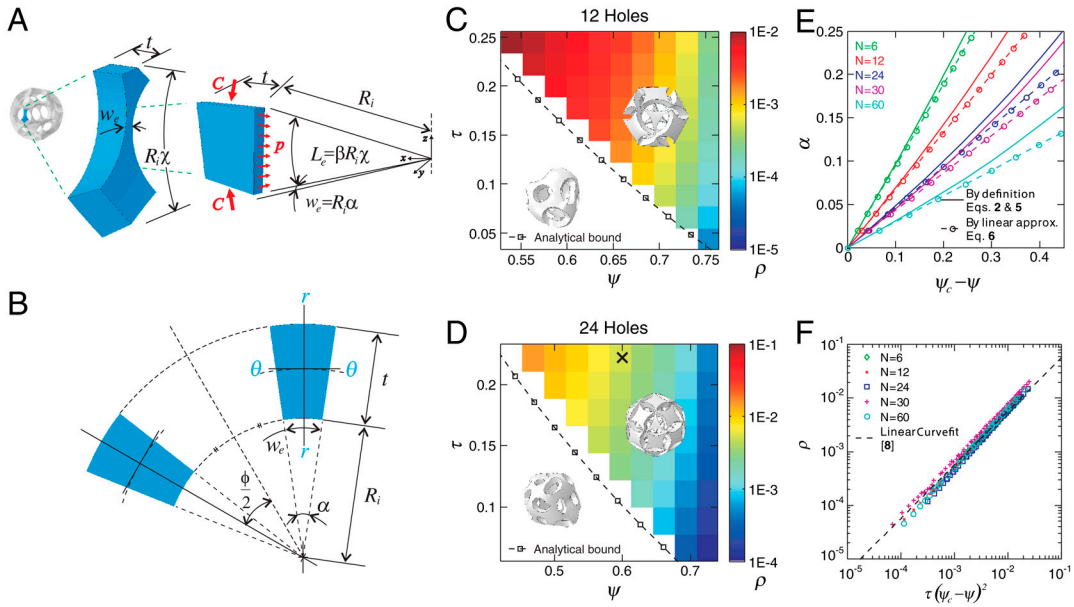

Fig. 4. (*A*) Representative ligament (*Center*) extracted from the Buckliball, and a simplified curved column model (*Right*). (*B*) Narrowest cross-section of the ligament. (*C* and *D*) Phase diagram of the two design parameters $\langle \tau = t/R_i, \psi\rangle$. The color-shaded region indicates on-sphere buckling and the white region represents the out-of-sphere buckling. The magnitude of the critical pressure for the onset of the on-sphere buckling is shown as a contour map with the adjacent color bar; (*C*) for 12 holes and (*D*) for 24 holes. The dotted marked lines indicate the analytical criterion from Eq. **3**, based on the second moment of area. (*E*) Linear approximation of the normalized effective width of the ligament ($\alpha = w_e/R_i$, see [**8**]) in terms of effective solid volume fraction ($\psi_c - \psi$). This linear approximation is valid up to the width ratio of $\alpha \approx 0.15$. (*F*) Master curve obtained from the buckling of the simplified ligament shapes. Regardless of the hole arrangements, the normalized critical pressure ($\rho = p/E$) for the onset of on-sphere buckling has a distinctive relation with the two design variables $\langle \tau, \psi\rangle$, $\rho \approx A\tau(\psi_c - \psi)^2$, with the prefactor $A = 0.556$ and a coefficient of determination of $\mathcal{R}^2 = 0.998$.

moment of area of the narrowest cross-section of the ligaments. Because our criterion does not consider the ligament curvature (which can favor the out-of-sphere buckling), it may provide a slightly less conservative design space of the buckling for encapsulation, which is, nonetheless, still in good agreement with the FE simulation results.

In addition, we explored the effect of geometric defects (unavoidable during fabrication) and performed an additional set of simulations accounting for imperfections, as summarized in the *SI Text*. These simulations demonstrate that the on-sphere buckling of the Buckliball leading to the desired encapsulation feature is robust and not affected by moderate levels of imperfections.

Design Master Curve for Encapsulation

We now provide a single master curve for the rational design of the Buckliball toward encapsulation applications. Thus far we have shown that, despite their complex overall geometry, the behavior of our Buckliballs is primarily governed by the geometry of the narrow ligaments of the shell. We proceed by considering the narrowest part of the ligament shown in Fig. 4*A*. Using the force equilibrium at each individual ligament, we can obtain an approximate relation between the compressive load C acting on its two ends and the pressure p applied to its inner surface,

$$C \approx R_i^2 \alpha p, \qquad [4]$$

which is valid for small values of α (i.e., large porosity) because we employ the linear approximation $\sin\alpha \approx \alpha$ (see *SI Text* for derivation).

To simplify our analysis, the shape of the selected part of the narrow ligament is further approximated by a curved column with dimensions t, L_e, and w_e (see schematic diagram in Fig. 4*A*). Here, the effective width of the ligament (w_e) and the effective column length (L_e) are defined as

$$w_e = R_i\alpha \quad \text{and} \quad L_e = \beta R_i \chi, \qquad [5]$$

where χ is the angle between two vectors which originate at the shell center and terminate at the center of the two neighboring solid parts of a expanded polyhedron (see Fig. 4*A*), and $\beta \in (0, 1]$ is a prefactor relating the ligament length to the effective column length. Note that the angle χ is fixed for a particular hole configuration. The possible pairs $\langle N, \chi\rangle$ for the five configurations are $\langle 6, \cos^{-1}(\frac{1}{3})\rangle$, $\langle 12, \cos^{-1}(\frac{1}{\sqrt{3}})\rangle$, $\left\langle 24, \frac{\pi}{4} \text{ and } \cos^{-1}\left(\sqrt{\frac{2}{3}}\right)\right\rangle$, $\left\langle 30, \cos^{-1}\left(\sqrt{\frac{5+2\sqrt{5}}{15}}\right)\right\rangle$, and $\langle 60, \cos^{-1}\left(\sqrt{\frac{3+\sqrt{5}}{6}}\right) \text{ and } \cos^{-1}\left(\sqrt{\frac{5+\sqrt{5}}{10}}\right)$ reflecting that Buckliballs with 24 and 60 holes have two types of ligaments with slightly different lengths. Substituting w_e and L_e (Eq. **5**) into Euler's buckling equation for a single ligament yields

$$C_{\text{cr}} = \frac{\pi^2 E t w_e^3}{12 L_e^2} \approx \frac{\pi^2 E t R_i \alpha^3}{12\beta^2\chi^2}. \qquad [6]$$

Combining this critical buckling load for a single ligament (Eq. **6**) with the pressure-induced compressive load applied to the ligaments (Eq. **4**), we obtain an expression for the normalized buckling pressure (denoted by $\rho = p_{cr}/E$) in terms of τ and α,

$$\rho \approx \frac{\pi^2}{12\beta^2\chi^2}\tau\alpha^2. \qquad [7]$$

The angle α defining the narrowest width of the ligament is a nonlinear function of void volume fraction ψ, as shown in Eq. **2**, which upon Taylor's series expansion allows us to express the angle α as a linear function of ψ near ψ_c :

$$\alpha \approx \frac{2}{\sqrt{\psi_c(N-\psi_c)}}(\psi_c - \psi), \qquad [8]$$

where ψ_c denotes a critical void volume fraction, beyond which the narrowest thickness of the ligaments vanishes (i.e., $\alpha = 0$ in Eq. **2**) and the spherical shell loses structural integrity. The specific hole arrangement, alone, sets the value of ψ_c (see Eq. **2**). In Fig. 4*E* we plot the angle α as a function of $(\psi_c - \psi)$, which confirms the validity the linear approximation in [**8**] for structures characterized by large values of porosity (i.e., small α).

Finally, substituting [**8**] into [**7**] provides a relation between the normalized buckling pressure ρ and the two design parameters τ and ψ,

$$\rho \approx A\tau(\psi_c - \psi)^2, \qquad [9]$$

where the coefficient $A = \pi^2[3\beta^2\chi^2\psi_c(N-\psi_c)]^{-1}$ is a weak function of hole arrangement. In Fig. 4*F* we plot ρ versus $A(\psi_c - \psi)^2$ for all of the numerical runs (over 250) from the five hole configurations, including the previous parametric study (Fig. 4 *C* and *D*). All of the data collapse onto a linear master curve with a prefactor of $A = 0.556$ (coefficient of determination $\mathcal{R}^2 = 0.998$), which confirms our predictions in [**9**]. In addition, from the identified value of the prefactor A, we can inversely calculate the prefactor β for all the five hole configurations, finding that its mean value is $\langle\beta\rangle = 0.839$.

Despite the a priori complex geometry of the Buckliball, this master curve indicates that, regardless of the hole arrangement, the encapsulation behavior of the ball is indeed dictated by the buckling of ligaments of the shells. Our analysis provides us with two practical guidelines for the design of the Buckliball. The first (Eq. **3** shown in Fig. 4 *C* and *D*) sets the shell dimensions required for buckling-induced encapsulation. Secondly, the master curve ([**9**] shown in Fig. 4*F*) provides an estimation for the critical buckling pressure for actuation of the Buckliball with given dimensions and for a particular hole arrangement. During this design procedure, the fabrication constraint can be explored by checking the smallest dimension of the ball, which is the narrowest cross-section of ligament ([**8**] shown in Fig. 4*E*) for the given porosity and hole arrangement.

Conclusion

We have introduced the Buckliball, a class of continuum elastic shells structures, which exhibits encapsulation through folding that is induced by buckling under pressure loading. An important advantage of our system is that it is made of a single continuum structure, which eliminates the need for a large number of hinges and rotating elements required in typical foldable/deployable structures. We chose pressure as the actuation mechanism and concentrated on macroscopic length scales for the sake of experimental convenience and accurate control. We then focused our analysis on the loading of the Buckliball's skeleton without membranes to aim for further generality of the results.

Our combined experimental, numerical, and theoretical approach allowed us to rationalize the underlying mechanical ingredients and yielded a series of simple design guidelines, including a master curve, for buckling-induced encapsulation. Moreover, because the folding mechanism exploits a mechanical instability that is general, our study raises the possibility for reversible, tunable, and controllable encapsulation, over a wide range of length scales. Recent developments in microscale fabrication open exciting opportunities for miniaturization of the Buckliball, for example, using projection microstereo lithography (33) or galvanic exchange-coupled Kirkendall growth (34) to produced patterned hollow particles. Our study therefore opens avenues for encapsulation at the microscale using other forms of loading, such as bilayer structures (e.g., unshrinkable outer ball attached to shrinkable inner ball) having swelling/shrinking actuation

under various external stimuli including pH, temperature, and water content, toward practical applications.

Materials and Methods

Materials. A silicone-based rubber (Elite Double 32; Zhermack) was used to cast the experimental specimen. The material properties were measured through tensile testing, up to the true strain of $\epsilon = 0.6$. No hysteresis was found during loading and unloading. The constitute behavior was accurately captured by a Yeoh hyperelastic model (35), whose strain energy is $U = \sum_{i=1}^{3} C_{i0}(\bar{I}_1 - 3)^i + (J-1)^{2i}/D_i$ where $C_{10} = 131$, $C_{20} = 0$, $C_{30} = 3.5$ kPa, and $D_1 = D_2 = D_3 = 38.2$ GPa^{-1}. Here, $\bar{I}_1 = \mathrm{tr}[\mathrm{dev}(\mathbf{F}^T\mathbf{F})]$, $J = \det[\mathbf{F}]$, and $\mathbf{F}$ is the deformation gradient. Two of the Yeoh model parameters are related to the conventional shear modulus (G_0) and bulk modulus (K_0) at zero strain: $C_{10} = G_0/2$, $D_1 = 2/K_0$.

Spherical Shell Specimen. A mold was fabricated using a 3D printer (Elite Printer; Dimension) to cast one-half of a spherical shell. After demolding, two halves were joined using the same polymer as adhesive agent. Note that the continuum shell and the thin membrane are constructed as a single piece. The coordinates of the holes were obtained from the vertices of the corresponding polyhedron, and the geometry of each hole was designed such that the hole portion is cut out from the spherical shell by a cone whose vertex is at the center of the sphere. A thin membrane located at the inner radius covered all the holes, thereby making the shell airtight. In order to extract the air from the shell, a 2-mm inlet was introduced at the shell's base and connected to the syringe through silicone tubing. The ball dimensions were as follows: inner radius $R_i = 22.5$ mm, shell thickness $t = 5$ mm, membrane thickness $h = 0.4 \pm 0.1$ mm, void volume fraction $\psi = 0.6$. Note that the variation of the measured membrane thickness reflects the resolution (0.1 mm) of the 3D printer used to make the molds. In addition, we introduced tapered fillets (between the membranes and the skeleton) to the samples to prevent the membranes from being damaged during the demolding procedure (the fillet radius is 1.0 mm), and we applied extra material both to the hemispherical joints to connect two hemispheres and to the thin membranes to make them airtight, so increasing the stiffness of the samples.

Pressure Testing and Analysis. The pressure-driven experimental setup was comprised of a syringe (BD 60CC Irrigation Syringe; Becton Dickinson), a syringe pump (NE-1000 Single Syringe Pump; New Era Pump Systems, Inc.), a pressure gauge (MPXV4115VC6U-ND; Digi-Key), silicone tubing (51135K84; McMaster-Carr), and a camera (D90; Nikon). During the withdrawal of the syringe pump (average rate of 0.1 mm^3/s), pictures taken with the camera and pressure values were digitized (0.1 Hz acquisition rate). The total duration of an experimental run was approximately 10 min. The rotation of the spherical shell was monitored by tracking four black dots on top of the shell. In parallel, the outer radius of the shell was estimated by measuring its projected area. Both the rotation of the ligaments and the change of the shell diameter were analyzed by digital image processing using Matlab.

Numerical Simulations. The commercial FE software Abaqus FEA was used for both buckling and postbuckling analysis. The Abaqus/Standard solver was employed for all the simulations—i.e., for both buckling and postbuckling analysis. For the buckling analyses of the Buckliball without membranes covering the holes, models were built using quadratic solid elements (Abaqus element type C3D10MH with a mesh sweeping seed size of 2.5 mm) and the analyses were performed under pressure loading. For the postbuckling analysis, the membrane covering the holes was included in the model and the simulations were performed under volume-controlled conditions. Both the skeleton and the membranes were modeled using quadratic solid elements (element type C3D10MH with a mesh sweeping seed size of 2.5 mm). To perform the simulation under volume-control conditions, the Buckliball was modeled as a spherical shell filled with fluid employing hydrostatic fluid elements (F3D3 with a mesh sweeping seed size of 1.25 mm). The fluid was assumed to be compressible air having a density of 1.204 kg/m^3 at 20 °C, and its volume was progressively reduced during simulations. More details on the FE simulations are provided in the *SI Text*.

ACKNOWLEDGMENTS. We are grateful to Zorana Zeravcic for helpful discussions, and to Harvard School of Engineering and Applied Sciences Academic Computing for their support. This work has been partially supported by the Harvard Materials Research Science and Engineering Center under National Science Foundation Award DMR-0820484 and by the MIT-France program. K.B. acknowledges startup funds from the School of Engineering and Applied Sciences, Harvard and the support of the Kavli Institute at Harvard University. P.M.R. acknowledges startup funds from the Departments of Mechanical Engineering and Civil and Environmental Engineering, MIT.

1. Ocampo JMZ, et al. (2003) Optical actuation of micromirrors fabricated by the microorigami technique. *Appl Phys Lett* 83:3647–3649.
2. Li XL (2008) Strain induced semiconductor nanotubes: From formation process to device applications. *J Phys D Appl Phys* 41:193001.
3. van Honschoten JW, et al. (2010) Elastocapillary fabrication of three-dimensional microstructures. *Appl Phys Lett* 97:014103.
4. Caruso F, Caruso RA, Möhwald H (1998) Nanoengineering of inorganic and hybrid hollow spheres by collodial templating. *Science* 282:1111–1114.
5. Peyratout CS, Dahne L (2004) Tailor-made polyelectrolyte microcapsules: From multilayers to smart containers. *Angew Chem Int Edit Engl* 43:3762–3783.
6. Suh WH, Jang AR, Suh YH, Suslick KS (2006) Porous, hollow, and ball-in-ball metal oxide microspheres: Preparation, endocytosis, and cytotoxicity. *Adv Mater* 18:1832–1837.
7. Shiomi T, et al. (2009) Synthesis of a cagelike hollow aluminosilicate with vermiculate micro-through-holes and its application to ship-in-bottle encapsulation of protein. *Small* 5:67–71.
8. Zhu YF, et al. (2005) Stimuli-responsive controlled drug release from a hollow mesoporous silica sphere/polyelectrolyte multilayer core-shell structure. *Angew Chem Int Edit Engl* 44:5083–5087.
9. Ren N, et al. (2004) Mesoporous microcapsules with noble metal or noble metal oxide shells and their application in electrocatalysis. *J Mater Chem* 14:3548–3552.
10. Hao E, et al. (2004) Optical Properties of Metal Nanoshells. *J Phys Chem B* 108:1224–1229.
11. Martinez CJ, Hockey B, Montgomery CB, Semancik S (2005) Porous tin oxide nanostructured microspheres for sensor applications. *Langmuir* 21:7937–7944.
12. Kornbluh R, Peirine R, Pei Q, Oh S, Joseph J (2000) Ultrahigh strain response of field-actuated elastomeric polymers. *Proc SPIE* 3987:51–64.
13. Oh KW, Ahn CH (2006) A review of microvalves. *J Micromech Microeng* 16:R13–R39.
14. Forterre Y, Skotheim JM, Dumais J, Mahadevan L (2005) How the Venus flytrap snaps. *Nature* 433:421–425.
15. Skotheim JM, Mahadevan L (2005) Physical limits and design principles for plant and fungal movements. *Science* 308:1308–1310.
16. Lee H, Xia C, Fang NX (2010) First jump of microgel; actuation speed enhancement by elastic instability. *Soft Matter* 6:4342–4345.
17. Baker TS, Olson NH, Fuller SD (1999) Adding the third dimension to virus life cycles: Three-dimensional reconstruction of icosahedral viruses from cryo-electron micrographs. *Microbiol Mol Biol Rev* 63:862–922.
18. Speir JA, Munshi S, Wang G, Baker TS, Johnson JE (1995) Structures of the native and swollen forms of cowpea chlorotic mottle virus determined by X-ray crystallography and cryo-electron microscopy. *Structure* 3:63–78.
19. Douglas T, Young M (1998) Host-guest encapsulation of materials by assembled virus protein cages. *Nature* 393:152–155.
20. Kovács F, Tarnai T, Fowler PW, Guest SD (2004) A class of expandable polyhedral structures. *Int J Solids Struct* 41:1119–1137.
21. Kovács F, Tarnai T, Guest SD, Gowler PW (2004) Double-link expandohedra: A mechanical model for expansion of a virus. *Proc R Soc London A Math Phys* 460:3192–3202.
22. Fuller RB (1982) *Synergetics: Explorations in the Geometry of Thinking* (MacMillan, New York).
23. Stuart RD (1963) *Polyhedral and Mosaic Transformations* (Student Publications of the School of Design, North Carolina State University, Raleigh, NC).
24. Clinton JD (1971) Advanced structural geometry studies. Part 2: A geometric transformation concept for expanding rigid structures. (NASA, Washington, DC) Report CR-1735.
25. Verheyen F (1989) The complete set of Jitterbug transformers and the analysis of their motion. *Comput Math Appl* 17:203–250.
26. Hoberman C (1990) Reversibly expandable doubly-curved truss structure. US Patent 4942700.
27. Bertoldi K, Reis PM, Willshaw S, Mullin T (2009) Negative Poisson's ratio behavior induced by an elastic instability. *Adv Mater* 22:361–366.
28. Kroto HW, Heath JR, O'Brien SC, Curl RF, Smalley RE (1985) C60: Buckminster-fullerene. *Nature* 318:162–163.
29. Li B, Cao YP, Feng XQ, Gao H (2011) Surface wrikling patterns on a core-shell soft sphere. *Phys Rev Lett* 106:234301.
30. Hutchinson JW (1967) Imperfection sensitivity of externally pressurized spherical shells. *J Appl Mech* 34:49–55.
31. Carlson RL, Sendelbeck RL, Hoff NJ (1967) Experimental studies of the buckling of complete spherical shells. *Exp Mech* 7:281–288.
32. Cromwell PR (1997) *Polyhedra* (Cambridge Univ Press, Cambridge, UK).
33. Sun C, Fang N, Wu DM, Zhang X (2005) Projection micro-stereolithography using digital micro-mirror dynamic mask. *Sens Actuators A Phys* 121:113–120.
34. González E, Arbiol J, Puntes VF (2011) Carving at the nanoscale: Sequential galvanic exchange and Kirkendall growth at room temperature. *Science* 334:1377–1380.
35. Yeoh OH (1993) Some forms of the strain energy function for rubber. *Rubber Chem Technol* 66:754–771.

Supporting Information

Shim et al. 10.1073/pnas.1115674109

SI Text

Derivation of Equation for Void-Volume Fraction, Eq. 2. To clarify the derivation of Eq. **2** in the main manuscript, we focus on the simplest case of the Buckliball with six voids (Fig. S1), although the argument is general and applicable to all other four configurations.

We start by deriving the relation between the angles (ϕ, θ and α) used in Eq. **2** of the main manuscript. We define ϕ as the angle between two vectors, which originate at the shell center and terminate at two neighboring vertices of a folded polyhedron (see the schematic diagram in Fig. S1*A*). Because the void's center in the expanded polyhedron (i.e., cuboctahedron for this specific case) is placed at the vertex locations of the folded polyhedron (i.e., octahedron for this specific case), ϕ also represents the angle relating the center-to-center distance between two adjacent circular voids in the expanded polyhedron. In addition, we define α as the angle that sets the narrowest width of the ligament (Fig. S1*B*), and θ as the angle that sets the diameter of the void (Fig. S1*B*). From geometry, we obtain

$$\theta = \phi - \alpha. \qquad \textbf{[S1]}$$

Secondly, we calculate the volume of the intact spherical shell:

$$V_{\text{shell}} = \frac{4}{3}\pi[R_o^3 - R_i^3], \qquad \textbf{[S2]}$$

where R_i and R_o denote the inner and outer radius of the shell, respectively.

We now need to calculate the volume of a single void on the spherical shell (Fig. S1*D*). Because each void is defined by a cone of opening angle θ and vertex located at the center of the sphere (Fig. S1*C*), its volume is given by

$$V_{\text{void}} = \frac{2}{3}\pi[R_o^3 - R_i^3]\left[1 - \cos\left(\frac{\theta}{2}\right)\right]. \qquad \textbf{[S3]}$$

Finally, combining Eqs. **S1**–**S3**, we obtain the following expression for the void-volume-fraction,

$$\psi = \frac{NV_{\text{void}}}{V_{\text{shell}}} = \frac{N}{2}\left[1 - \cos\left(\frac{\phi - \alpha}{2}\right)\right], \qquad \textbf{[S4]}$$

which corresponds to Eq. **2** in the main manuscript.

Phase Diagrams of Design Parameters $\langle\tau,\psi\rangle$. We present additional phase diagrams of design parameters for shells with 6, 30, and 60 holes, which are not included in Fig. 4 of the main manuscript because of the page limitation.

Because the experiments suggest that the narrowest cross-section of ligament in the expanded status of the spherical shells governs the on-sphere buckling behavior of the balls, by comparing the second moment of area along two axes (i.e., $I_{rr} \le I_{\theta\theta}$) we obtain a relation between the two design parameters $\langle\tau, \psi\rangle$ (Eqs. **2** and **3** in the main manuscript). The corresponding phase boundary is plotted as a marked line in Fig. S2. In addition, to assess our predictions, we perform a series of finite element simulations where we investigate the buckling of Buckliball characterized by different pairs of the design parameters $\langle\tau, \psi\rangle$. The phase diagrams for shells with 6, 30, and 60 holes are presented in Fig. S2. In these phase diagrams, regions where out-of-sphere (snap) buckling occurs are represented in white. In the shaded regions where encapsulation (i.e., on-sphere buckling) occurs, the color in the contour plots represents the associated critical buckling pressure for onset of on-sphere buckling (normalized by the Young's modulus E), given by the adjacent color bar. We find that the contour map boundary between the regions of on-sphere and out-of-sphere buckling is in good agreement with our analytical prediction based on the second moment of area of the narrowest cross-section of ligament.

Derivation of Equation for Pressure-Compression Relation, [4]. We proceed by presenting a detailed derivation of the scaling in [**4**] in the main manuscript (Eq. [**8**] in this document). We start by considering a single ligament and simplify its geometrical description using a curved column with uniform width ($w_e = R_i\alpha$) and effective column length ($L_e = \beta R_i\chi$) (Fig. S3). In the main manuscript, [**4**] can be obtained from the force equilibrium along the radial direction for the simplified curved column. To simplify the derivation, let's orient the column so that the radial direction at the center of its width coincides with the x axis of the Cartesian coordinate (see Fig. S3, *Right*). Introducing a spherical coordinate system ($r > 0$, $\theta \in [0, \pi]$, $\varphi \in [0, 2\pi)$) so that $x = r\sin\theta\cos\varphi$, $y = r\sin\theta\sin\varphi$, and $z = r\cos\theta$, the component along the x direction (i.e., the radial direction) of the pressure p, denoted by F_x^p, can be obtained as

$$\begin{aligned} F_x^p &\approx \int_{\theta=\frac{\pi}{2}-\frac{\alpha}{2}}^{\theta=\frac{\pi}{2}+\frac{\alpha}{2}} \int_{\varphi=-\frac{\beta\chi}{2}}^{\varphi=\frac{\beta\chi}{2}} (p\sin\theta\cos\varphi)R_i^2\sin\theta d\theta d\varphi \\ &\approx pR_i^2[\alpha + \sin\alpha]\sin\left(\frac{\beta\chi}{2}\right). \end{aligned} \qquad \textbf{[S5]}$$

Because the component along the x direction of the compressive force C, denoted by F_x^C, is given by

$$F_x^C = 2C\sin\left(\frac{\beta\chi}{2}\right), \qquad \textbf{[S6]}$$

force equilibrium in the x direction (i.e., $F_x^p = F_x^C$) yields

$$pR_i^2[\alpha + \sin\alpha] = 2C. \qquad \textbf{[S7]}$$

For large values of porosity $\alpha \to 0$, so that we can use the approximation $\sin\alpha \approx \alpha$, and Eq. **S7** reduces to

$$C \approx R_i^2\alpha p, \qquad \textbf{[S8]}$$

which corresponds to [**4**] in the main manuscript.

Postbuckling Analysis: Finite Element Simulations. Because the buckling analysis performed using Abaqus/Standar solver reveals that linear continuum elements lead to strong mesh-size dependent behavior, we built all the models using quadratic continuum elements (C3D10MH: a quadratic hybrid-continuum element with a 10-node modified tetrahedron having one additional variable relating to pressure) for both the thin membranes and the skeleton (thicker parts) of the shells.

Note that continuum elements are also used for the membrane, to resolve issues of compatibility between the quadratic continuum elements and linear shell elements for large-strain formulations. Although Abaqus/Standard provides various conventional thin shell element types, only few shell elements are suitable for large-strain analysis (1); these are linear thin shell

element (e.g., S3(R), S4(R), etc.) and quadratic thick shell elements (e.g., SC8(R), etc.), which are also called continuum shell elements. Both element types have a compatibility issue with quadratic continuum element types of *C3D10M(H)* and therefore we decide to use continuum elements for both the thin membranes and the thicker parts of the shells.

To perform the postbuckling analysis under volume-controlled conditions, the Buckliball was modeled as a spherical shell filled with fluid for which we used hydrostatic fluid elements (F3D3 with a mesh sweeping seed size of 1.25 mm). The fluid has been assumed to be compressible air having a density of 1.024 kg/m^3 at 20 °C and its volume has been progressively reduced during the simulations. Because Abaqus/Standard provides only linear hydrostatic fluid elements (element type *F3D3*), the mesh for the fluid elements was designed such that four fluid elements (i.e., four *F3D3* elements) are attached to a single face of the quadratic solid element (i.e., *C3D10MH*). In addition, implicit dynamic analysis were performed using Newmark algorithm with $\beta = 0.276$ and $\gamma = 0.550$ (such conditions are achieved by setting $\alpha = -0.05$, "*DYNAMIC, ALPHA = −0.05"). Note that this damping is purely numerical and is different from the material damping (2). The kinetic energy was monitored during simulations and observed to be less than 3.0% of the strain energy, ensuring quasi-static conditions.

A mesh sweeping seed size of 2.5 mm was chosen for the solid elements, resulting in hydrostatic fluid elements of size that is roughly half the size of the solid elements due to the above-mentioned mesh design procedure. For example, the model used for the postbuckling analysis of the Buckliball with membrane thickness $h = 0.5$ mm has 15,469 *C3D10MH* elements and 8,704 *F3D3* elements (Fig. S4*A*). Fig. S4*C* shows the results of the postbuckling analysis performed under volume-controlled conditions, which are presented in the main manuscript. The computational cost of the simulation was remarkably high; a single postbuckling analysis under volume control took 40 h using 48 central processing units. This extremely high computational cost for the volume-control simulations hindered further investigation on the effect of mesh size and numerical damping parameter.

For the sake of computational convenience, the accuracy of the mesh used in the volume-control simulations was ascertained performing several simulations under pressure-controlled conditions, whose computational cost is found to be less than one-fifth of that of the volume-controlled simulations. Therefore, models with sweeping mesh sizes of up to 1.0 mm were built and tested (see Fig. S4*B*).

For the static analysis under pressure-controlled conditions, a stabilized scheme using artificial damping was employed because the postbuckling behavior of the Buckliball covered by a thin membrane is characterized by two different types of sequential unstable buckling events (i.e., local snap-buckling events in the thin membranes followed by a global buckling mode of the skeleton). Note that the Abaqus/Standard solver provides an automatic stabilization with artificial damping; where viscous forces of the form $F_v = cM^*v$ are added to the global equilibrium equations; here, c is a damping factor, M^* is an artificial mass matrix calculated with unit density, and v is the nodal velocity vector. We choose an option where the damping factor c is determined in such a way that the dissipated energy for a given increment is 0.02% of the extrapolated strain energy, which is the default value by using the Abaqus keyword "*STATIC, STABILIZE = 0.0002". When we reduce the damping factor below 0.02%, the simulation stops before capturing the local snap-buckling of membranes. Thus, the damping factor of 0.02% is the smallest value with which the numerical simulations were still able to capture the correct postbuckling behavior. More details on this automatic stabilization scheme are presented in ref. 3.

Comparison of the results from the volume-controlled simulations (with mesh sweeping size of 2.5 mm shown in Fig. S4*C*) and pressure-controlled simulations (with mesh sweeping size of 1.0 mm shown in Fig. S4*D*) shows good agreement in terms of initial linear response and critical buckling pressure. These results confirm that the mesh size used in the volume-controlled simulations is fine enough to accurately predict the onset of buckling and postbucking behavior. Moreover, although the pressure-controlled simulations were unable to capture the experimentally observed softening that follows immediately after the onset of buckling, this feature was accurately predicted by the volume-controlled simulations.

Effect of Geometric Imperfections. We have performed an additional set of simulations to explore the imperfection sensitivity of buckling for the Buckliball, focusing on the Buckliball with 24 voids. The Buckliball had an inner radius $R_i = 22.5$ mm, shell thickness $t = 5$ mm, void-volume fraction $\psi = 58.7\%$, and the voids were not covered by a membrane. For this given Buckliball design, we introduced imperfections in the form of different void size and misplaced void location on the sphere when compared to their geometrically exact set by the underlying polyhedron. We explored the response of structures with stochastically displaced and sized voids of amplitude $a = 1\%t$, $5\%t$, $10\%t$, and $15\%t$ (i.e., $t = 5$ mm). Note that, for imperfections of magnitude larger than $15\%t$, the narrowest width of ligament vanishes so that the Buckliball loses structural integrity. Five configurations are generated and tested for each value of a, totaling 20 sets of simulations for both buckling and postbuckling analysis. The dependence of the critical buckling load as a function of a is presented in Fig. S5, showing that the critical pressure tends to decrease as the magnitude of imperfection increases. In addition, representative snapshots from the postbuckling analysis are shown in Fig. S6. For the cases with $a = 1\%t$ and $5\%t$, the pressure at the onset of buckling is found to be only marginally affected by imperfection (less than 1%) and all five configurations show a nearly perfect on-sphere buckling leading to the desired encapsulation behavior, and therefore only one representative snapshot is reported (Fig. S6 *A* and *B*). On the other hand, various postbuckled shapes are observed for the cases of $a = 10\%t$ and $15\%t$ and three representative snapshots are presented for each case (Fig. S6 *C* and *D*). As the magnitude of imperfection increases, the width of the ligaments of the Buckliball is strongly affected by the imperfections, so that the deformation tends to localize within the narrowest ligaments. For $a = 10\%t$, all five Bucklballs show the desired encapsulation postbuckling behavior, albeit with postbuckled shapes that can deviate from a sphere (Fig. S6*C*). Moreover, the pressure at buckling is reduced by roughly 7%. Finally, for $a = 15\%t$, the imperfection is found to strongly affect the response of the structures so that only one configuration out of five shows an encapsulation postbuckling behavior (Fig. S6*D*) and the critical pressure is now reduced by approximately 15%.

This additional set of simulations demonstrates that the encapsulation mechanism of the Bucklballs is robust and not affected by geometric imperfections up to $a = 10\%t$.

1. Abaqus (2008) *Abaqus Analysis User's Manual, Ver 6.8* (Dassault Systèmes Simulia Corp., Providence, RI), Sect 28.6.
2. Abaqus (2008) *Abaqus Theory Manual, Ver 6.8* (Dassault Systèmes Simulia Corp., Providence, RI), Sect 2.4.
3. Abaqus (2008) *Abaqus Analysis User's Manual, Ver 6.8* (Dassault Systèmes Simulia Corp., Providence, RI), Sect 7.1.

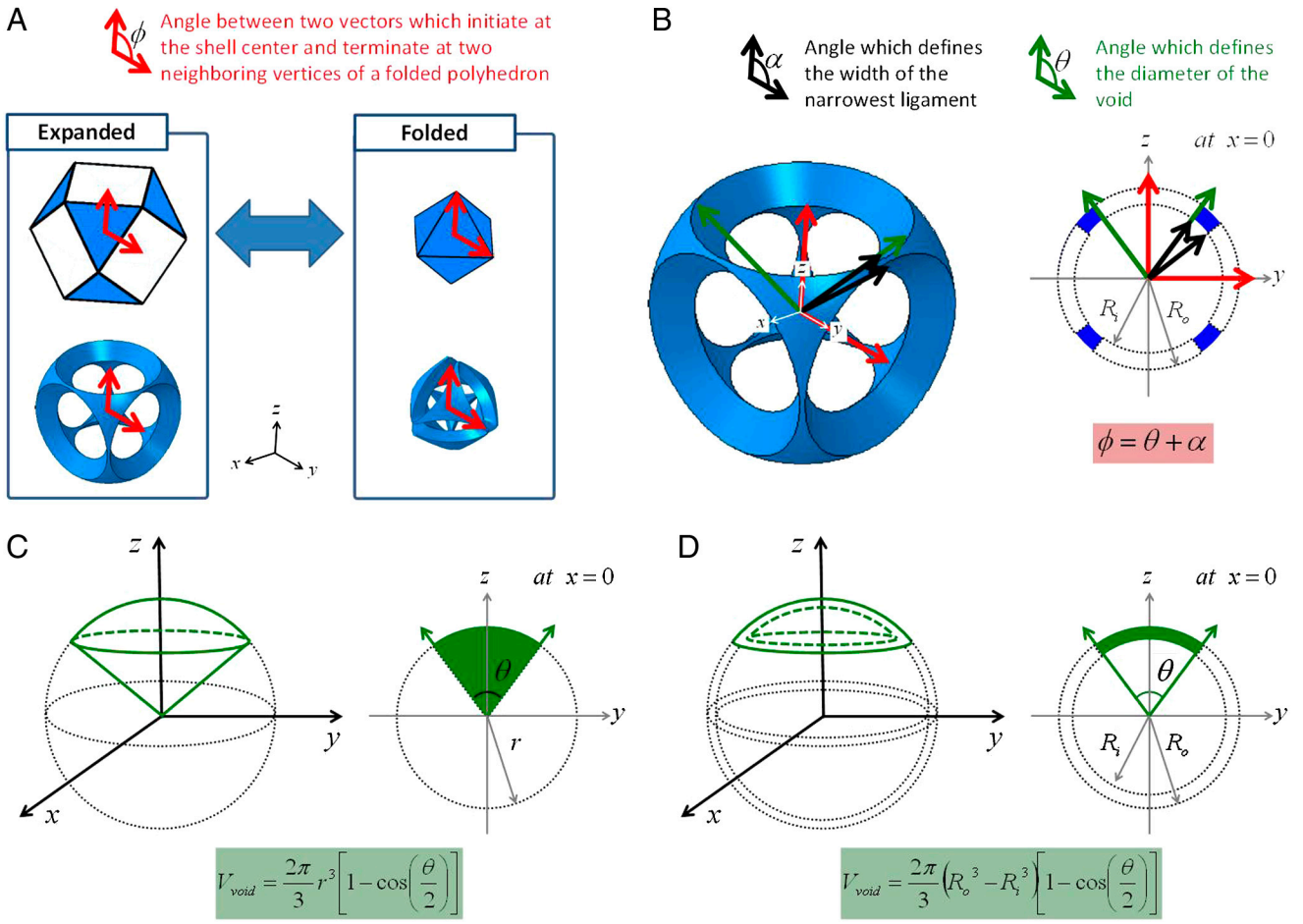

Fig. S1. Schematics illustrating (*A*) ϕ, (*B*) $\alpha$and θ, (*C*) a cone describing the hole on the spherical surface, and (*D*) the volume of each hole.

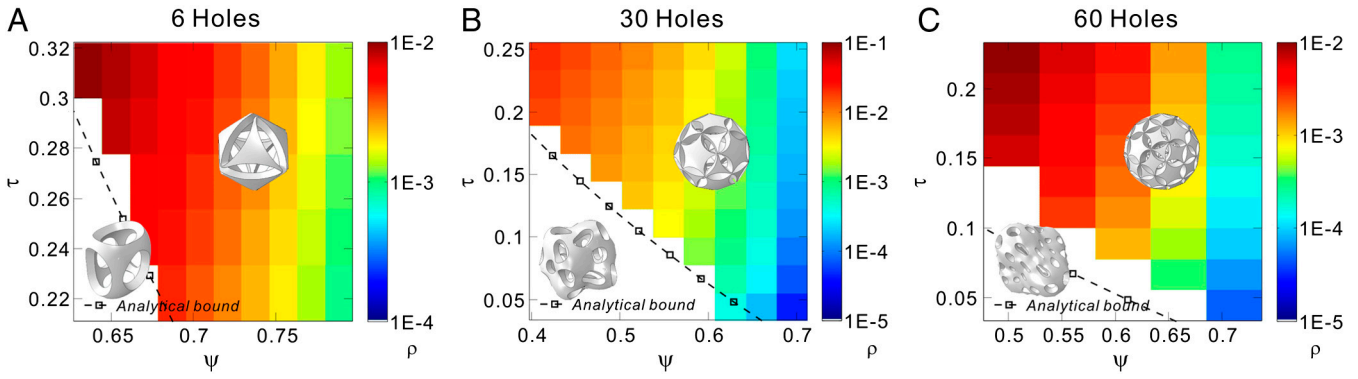

Fig. S2. Phase diagram of the two design parameters $\langle \tau, \psi \rangle$. The color-shaded region indicates on-sphere buckling and the white region represents the out-of-sphere buckling. The magnitude of the critical pressure for the onset of the on-sphere buckling is shown as a contour map with the adjacent color bar; (*A*) for 6 holes, (*B*) for 30 holes, and (*C*) for 60 holes.

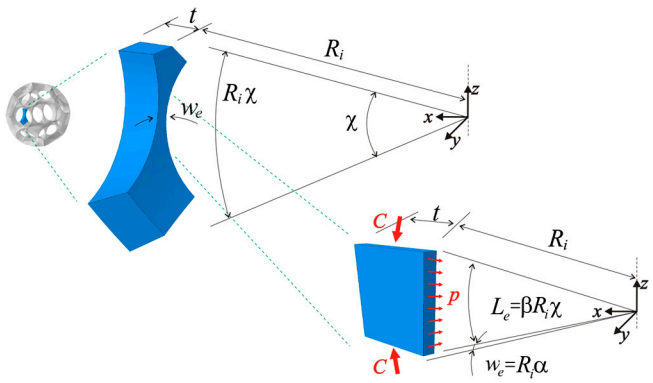

Fig. S3. Representative ligament extracted from the Buckliball and simplified curved column used in its buckling analysis.

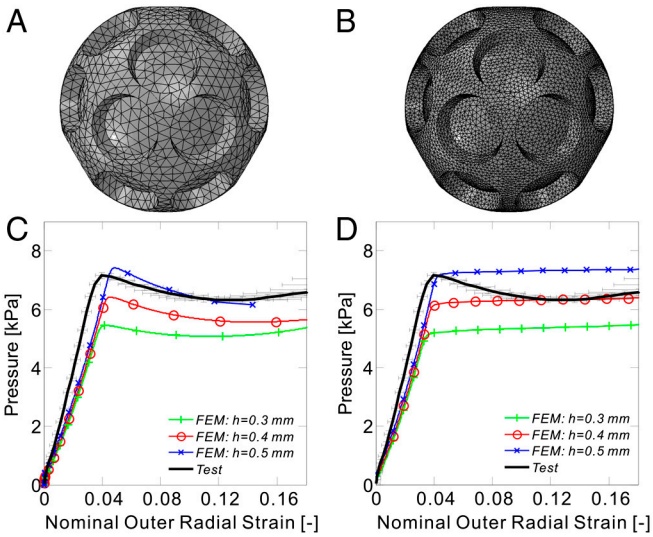

Fig. S4. (*A* and *B*) Meshed Buckliball with sweeping mesh size of (*A*) 2.5 mm and (*B*) 1.0 mm. (*C* and *D*) Dependence of the differential pressure of the ball on the nominal outer radial strain. Simulation results using finite element modeling (FEM), which are denoted by marked color lines, are obtained from (*C*) volume-controlled and (*D*) pressure-controlled conditions.

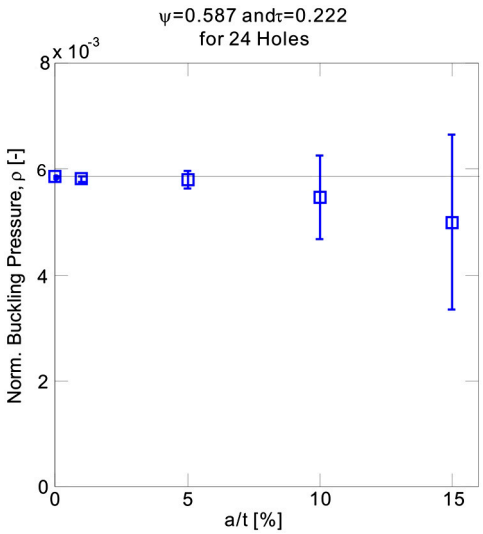

Fig. S5. Effect of imperfections on the normalized critical buckling pressure $\rho = p/E$. Blue square marks correspond to the mean value of five configurations and the size of error bar corresponds to the one-standard deviation. In addition, the black horizontal line represents the normalized critical buckling pressure for Buckliball without imperfections.

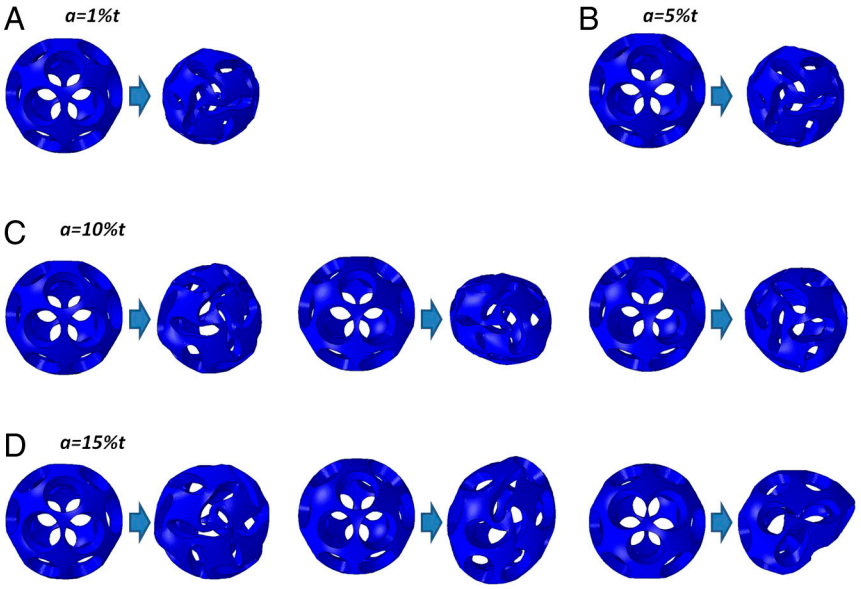

Fig. S6. Representative snapshots from the postbuckling analysis; (*A*) $a = 1\%t$ and (*B*) $a = 5\%t$. All five configurations remain spherical after buckling and show the encapsulation features. (*C*) For $a = 10\%t$, all five configurations show encapsulation features although after buckling their shapes significantly deviate from a sphere. (*D*) For $a = 15\%t$, only one configuration shows encapsulation features (*Left*), whereas all the others lead to irregularly collapsed shapes (*Center* and *Right*).